Article

Annular Electromagnetic Generator for Harvesting Ocean Wave Energy

Chunjie Wang [1,2], Linghao Guo [1,2], Peng Chen [1,2], Qiang Fu [1,2] and Lin Cui [3,*]

1   Tianjin Key Laboratory of New Energy Power Conversion, Transmission and Intelligent Control, Tianjin 300384, China; chunjie_wang@tjut.edu.cn (C.W.); glhtjut@stud.tjut.edu.cn (L.G.); chenpeng@email.tjut.edu.cn (P.C.); fuqiang@email.tjut.edu.cn (Q.F.)
2   School of Electrical Engineering and Automation, Tianjin University of Technology, Tianjin 300384, China
3   National Ocean Technology Center, Tianjin 300112, China
*   Correspondence: cuilin_oceanenergy@126.com

Abstract: To sustainably power ocean sensors by harvesting ocean wave energy, an annular electromagnetic generator (A-EMG) based on the principle of Faraday electromagnetic induction is proposed in this paper. The specific structure and working principle of the generator are introduced. The distribution of the magnetic field in the coil, the variation in the induced voltage and the influence of the coil parameters on the output were simulated by the COMSOL Multiphysics software version 6.0. At the same time, an experimental platform was built to test the output characteristics of the generator. Through a comparative study of the capacitor's charging characteristics, the optimal connection mode between the multiple groups of coils of the generator was preliminarily verified. Finally, the six-degree-of-freedom (6-DOF) platform was used to simulate various wave motion parameters, and the feasibility of the generator for supplying power to ocean sensors was verified.

Keywords: A-EMG; ocean sensors; COMSOL Multiphysics; ocean wave energy harvesting

1. Introduction

Ocean environmental monitoring is very important for the exploitation and utilization of ocean resources. Various types of ocean sensors are used to collect ocean environmental data, but there is always a lack of a reliable power supply in this field. At present, batteries, wind energy, solar energy, etc., are the most common power supply methods applied to ocean sensors. However, battery replacement is difficult and is often polluted, and solar and wind energy are both seriously affected by weather factors and their reliability is poor [1]. The ocean itself is rich in energy. In order to solve the bottleneck problem of supplying power, the most ideal way of supplying power is undoubtedly to be able to use the energy in the ocean [2–4]. Many wave-energy-harvesting devices have already been proposed and designed, and the most widely used method of wave energy harvesting is based on rotating electromagnetic generators (EMG). In other words, in these generators, wave energy is converted into mechanical energy, pneumatic energy or potential energy by the power take-off (PTO) device. The PTO is then connected to a rotating generator, and the energy is converted into electrical energy [5]. However, in recent years, with the rapid development of microelectronics, micro-electro-mechanical systems (MEMS) and mobile internet technologies, more and more sensors have widely been used in ocean equipment such as ocean environmental monitoring and position tracking. The traditional wave-energy-harvesting devices have the disadvantages of having a complex mechanical structure, they are easily corroded and they have high costs. In addition, these devices always have a large volume and a low energy harvesting efficiency, which is not suitable for powering ocean sensors [6]. Providing sustainable, low-cost and easy-to-maintain power energy for ocean sensors has become a major challenge. The development of energy-

harvesting devices with a small size and high output power is of great significance for the further development and application of various ocean devices [7].

As early as 2007, the American scholar Arnold, D.P. discussed the practical significance and feasibility of small electromagnetic generators, and he believes that small power supply devices are of great value for powering smart intelligent sensors, robots, wireless communication networks and other distributed microelectronic devices [8]. Harvesting energy from the environment is now increasingly becoming a promising method for powering small devices. Several studies have demonstrated the feasibility and superiority of small EMGs for harvesting energy from the surrounding environment [9]. Bowers et al. invented the rolling spherical magnet generator, which was used to harvest energy generated by human motion [10]. Samad et al. proposed a curved wearable electromagnetic energy harvesting system that can be used to harvest energy from the human body while walking or running from two directions [11]. Tu et al. invented a bistable vibration energy harvester based on spherical moving magnets for harvesting the vibration energy of a moving vehicle, which is applied to power safety detection equipment related to rail and road transportation [12]. Similarly, the research on the application of EMGs in wave energy harvesting is becoming more intensive, and more EMGs with different structures have been developed for wave energy harvesting. Wave energy harvesting is usually performed in an inertial pendulum structure [13,14], a gyroscopic structure or an eccentric structure [15,16]. Guo et al. proposed an eccentric pendulum structure consisting of a transmission gear and an electromagnetic power module, in which the pendulum converts low-frequency wave energy into mechanical rotational energy, and the transmission gear amplifies the low rotational speed of the pendulum. The electromagnetic power module is used to convert rotating mechanical energy into electrical energy. The maximum output power is 122 mW, and the output power density is 0.24 mW/cm^3 [17].

However, the horizontal single-axis pendulum structure can only harvest wave energy from a specific direction, and the wave direction of wave motion is always random, so it is more advantageous to harvest wave energy from multiple directions [18]. Lou et al. proposed a novel two-axis pendulum vibration energy harvester. Harvesting vibration energy based on oscillation is a promising energy-harvesting technology for buoys and small ocean vehicles. However, energy harvesters with a single-axis pendulum require the vibration excitation by the waves to be generated in a specific direction. A new vibration energy harvester for a two-axis pendulum has been developed. The hemispherical pendulum can rotate around two axes simultaneously to match to the direction of the vibration excitation. In addition, the magnets and coils are distributed on the surface of the pendulum and the housing, respectively, to achieve a compact structure, and its output can reach a peak voltage of 14.25 V and a power of 2.03 W under certain conditions [19]. Wang et al. proposed an EMG that simulates the motion of a dual hula-hoop for wave energy harvesting and presented a two-degree-of-freedom wave energy converter (WEC), which is a biaxial toroidal and eccentric generator composed of a circular Halbach array disk and an iron core coil. This WEC can convert the pitching, rolling and rotating motions of an unmoored buoy into electrical energy, and the device can output 0.56 W of power when the buoy's motion frequency is between 0.7 Hz and 1.0 Hz [20]. Carandell et al. proposed a kinetic energy harvester (KEH) applied to an ocean drifter, which combines a pendulum system with a gyroscope system. When waves act on the device, the relative motion is induced by an internal articulated arm, and it then drives a flywheel to drive a small generator via a gear system. When the external excitation reaches 1.5 Hz, its output power is 2 mW [21]. Pan et al. proposed a tumbler electromagnetic generator (T-EMG) with a Halbach array, in which coils, Halbach magnet units and magnetostrictive structures are installed in two hollow semi-elliptical enclosures. Under the conditions of adjusting the load to reach the optimal power matching point, a T-EMG has a maximum peak to peak voltage of 3 V and a maximum average output power of 65 mW under an external excitation of 2.6 Hz. In real wave environments of less than 1 Hz, its maximum peak power

reaches 120 mW, and it can successfully drive wireless temperature and humidity sensors and LEDs [22].

In order to achieve efficient and reliable energy harvesting for powering small marine equipment or sensors, an annular electromagnetic generator (A-EMG) is proposed in this paper. Compared with the structure proposed herein, in other existing works, such as in [21], the structures are more complex and are formed by a combination of a plurality of mechanical structures or by the connection of mechanical devices. The structures are also still relatively complex, and the more complex the structure is, the higher the probability of it malfunctioning, which may reduce the reliability of the device and reduce the energy conversion efficiency of.

The A-EMG proposed in this study only consists of a magnetic ball, an annular shell and three coils without any other mechanical structures and devices. The energy conversion process is simple; the wave motion that drives the movement of the magnetic ball can be converted into electricity, which improves the reliability of the device and reduces the energy loss. References [12,23], which are similar to the principle of the A-EMG, involve linear or curved tubes with a rolling magnetic ball that generate an induced current in separate winding coils. They place the magnetic ball in curved and straight tubes, respectively. When the magnetic ball moves to one end, the speed of the moment is reduced to 0, which undoubtedly increases the speed loss and energy loss, whereas the annular shell of the A-EMG allows for the continuous movement of the spherical magnet without any obstruction, which avoids the speed loss and energy loss to the greatest extent. The structure and working principle of the A-EMG are explained in this paper. The principle was simulated using the COMSOL Multiphysics software version 6.0, and the influence of the coil parameters on the output was analyzed. Finally, an experimental prototype was built, and the experiment was verified by using the six-degree-of-freedom (6-DOF) platform.

2. Structure Principle

As shown in Figure 1, the A-EMG consists of an annular shell, a magnetic ball that can move inside the annular shell and three groups of coils wrapped around the outer part of the annular shell at equal intervals. When the device is placed in an ocean environment, due to the fluctuating fluctuations of the ocean waves, the device will shake with the waves, thereby driving the magnetic ball to move. And when the magnetic ball passes through the coil, the magnetic flux changes, generating an induced electromotive force in the coil.
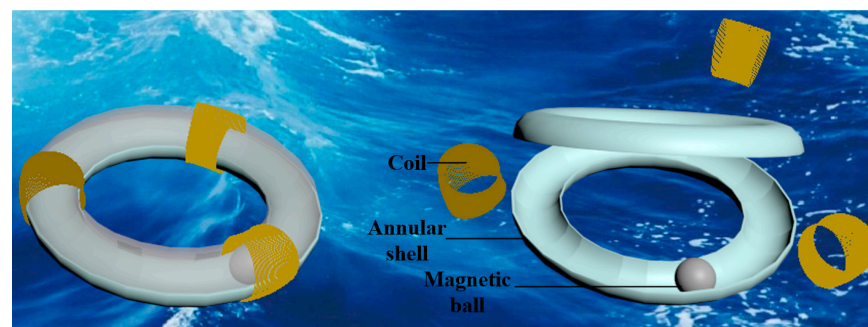

Figure 1. Three-dimensional structure of the A-EMG.

Figure 2 shows the working principle of the A-EMG. After being excited by a wave, the magnetic ball moves inside the annular shell, and according to the law of electromagnetic induction, the expression of the induced electromotive force can be obtained by using *V* to denote the induced electromotive force produced by the coil and Φ to denote the magnetic flux in one turn of the coil:
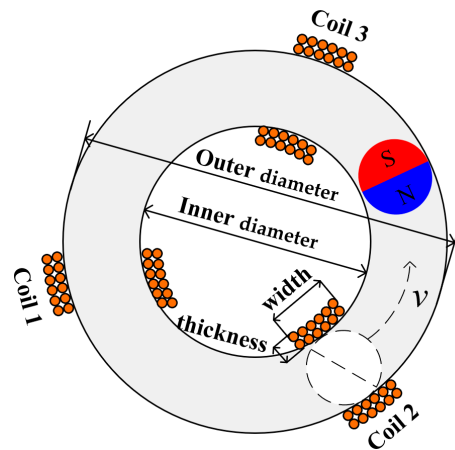
$$V = -N\frac{d\Phi}{dt} \tag{1}$$

Figure 2. Working principle of the A-EMG.

Assuming that the time for the spherical magnet to move inside the annular shell at the speed v is t and that the displacement of the movement is x, and denoting the magnetic flux density through the coil and the area of the coil by $B(x)$ and S, respectively, the induced electromotive force can be further expressed as:

$$V = -N\frac{d\Phi}{dt} = -NS\frac{dB(x)}{dx}\frac{dx}{dt} = -NS\frac{dB(x)}{dx}v \tag{2}$$

The angular velocity ω of the motion of the magnet ball can be expressed as:

$$\omega = \frac{v}{r} \tag{3}$$

The frequency f of the magnet ball moving around a ring can be expressed as:

$$f = \frac{1}{T} = \frac{1}{2\pi/\omega} = \frac{\omega}{2\pi} = \frac{v}{2\pi r} \tag{4}$$

Based on the above analysis, the relationship between the frequency and the induced electromotive force can be deduced:

$$V = -NS\frac{dB(x)}{dt}2\pi r f \tag{5}$$

According to Equation (2), it is clear that the magnitude of the induced voltage is related to the speed of motion of the magnetic ball through the coil; the faster the speed, the greater the induced voltage produced in the coil. From Equation (5), when the wave motion resonates with the ring generator, the magnetic ball will make a complete circular motion, and the induced voltage in the coil is related to the frequency of the circular motion, where the greater the frequency, the greater the induced electromotive force that is produced [24].

3. Principle Analysis and Parameter Effect Analysis Based on COMSOL

The working principle of the A-EMG was analyzed above. In order to further analyze and intuitively understand the working characteristics of the A-EMG, the COMSOL Multiphysics software was used to simulate and analyze the A-EMG. The parameter settings in the simulation are shown in Table 1. The A-EMG was modeled in a two-dimensional plane, and in the simulation, we set the outer diameter of the annular shell to 70 mm and the inner diameter to 35 mm. Considering that the larger the magnetic ball, the more favorable it is for the output power, and to ensure its movement in the annular shell, it was necessary to leave a certain air gap between the annular shell and the magnet ball. The diameter of the magnetic ball was set to 30 mm, the magnetic field module was selected as the simulation

background and the number of coil turns was set to 1000 turns. The variation in the flux density, magnetic field and induced voltage in the coil of the EMG section was investigated.

Table 1. Parameter settings in simulation.

Item	Value
Outer diameter × inner diameter of annular shell	140 mm × 70 mm
Magnetic ball diameter	30 mm
Turns of coil	1000

In the above principal explanation, we only considered the movement of the magnetic ball around the annular shell as "sliding" (the magnetic ball only moves around the annular shell, and the magnetic ball itself does not rotate). However, in reality, the magnetic ball may move in a "rolling" (the magnetic ball itself rotates) manner or in a combination of "sliding" and "rolling" during the process of passing through the coils. Similar to the references [23,25], we simulated and analyzed the magnetic field changes caused by the magnetic ball rotating 360° at a fixed position and the flux density transformation at point 1 on coil 1, as shown in Figure 3a. The protrusion on the annular shell in the figure indicates the coils set in the simulation. The simulation range was set to 0–360°, and the simulation step size was 5°.
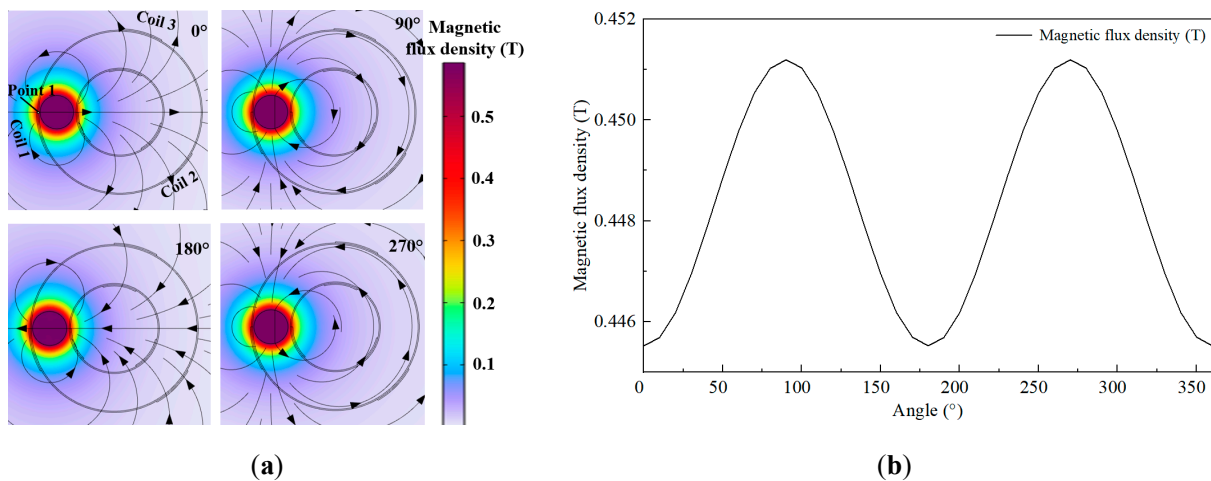

(**a**)   (**b**)

Figure 3. Magnetic field and flux density variations when magnetic ball is rotated in a fixed position. (**a**) The distribution of the magnetic field when the magnetic ball is in a different angle; (**b**) law of change in magnetic flux density at point 1 with the angle of the magnetic ball.

When the magnet ball rotates in the annular shell, it causes a change in the surrounding magnetic field and a change in the magnetic flux density at point 1 (same point as in Figure 3a). The simulation range was set to 0–360°, and the simulation step size was 5°. As shown in Figure 4, it can be seen that the motion of the magnet ball has an effect on the magnetic field and the flux produced.

Comparing Figure 3b with Figure 4b, it can be seen that the change in the magnetic flux density due to the rotation of the ball itself was not dominant compared to the movement of the ball around the annular shell, and considering that even if the ball passed through the coil in a "rolling" manner, the angle of rotation of the ball itself was difficult to determine. So, in the principle explanation and simulation, we simplified the motion form of the magnetic ball, ignored the rotation of the magnetic ball itself [26] and only considered the "sliding" motion of the magnetic ball.
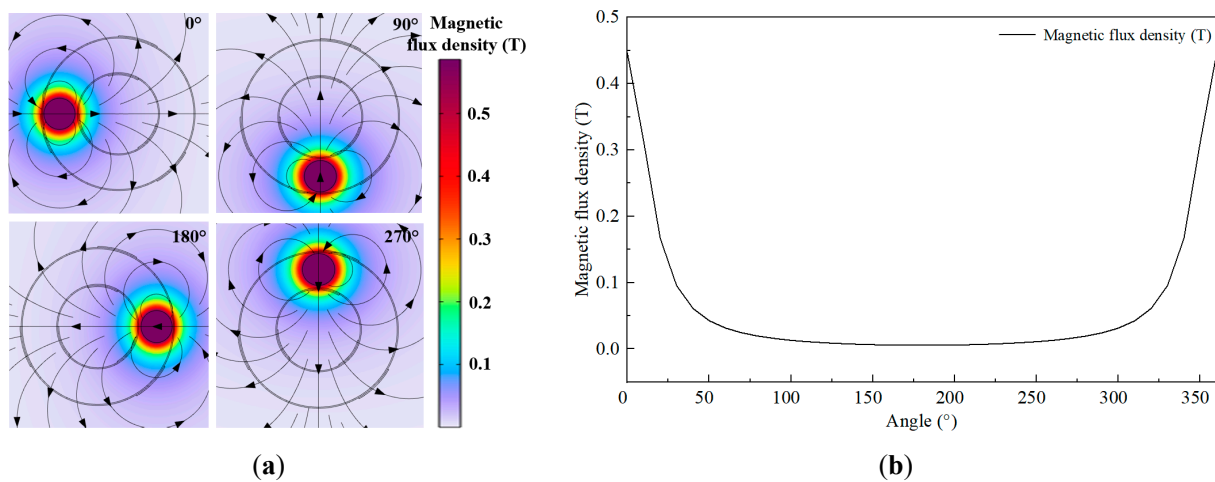
Figure 4. Magnetic field and flux density variations when magnetic ball is "sliding" around annular shell. (**a**) The distribution of the magnetic field when the magnetic ball is in different positions; (**b**) law of change in magnetic flux density at a point 1 with the position of the magnetic ball.

The induced electric potential generated in the coil when the magnetic ball moves in the annular shell at an angular velocity of 2π rad/s was studied and analyzed by using COMSOL. The simulation time was set to 5 s with a step of 0.1 s so as to verify the rule of change and the trend of the induced voltage in the coil during the passage of the magnetic ball through the coil. Figure 5 shows the induced electromotive force of the magnetic ball moving through the annular shell for five cycles, and in conjunction with Figure 4, it is clear that during a cycle, the magnetic flux in the coil increased as the ball rolled toward the coil and decreased as the ball moved away from the coil, generating a concomitant change in the electromotive force [23].
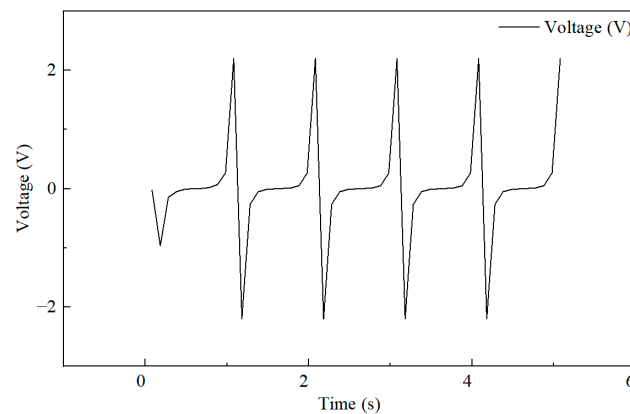

Figure 5. The law of change in the induced voltage in the coil.

The coil parameters have an important effect on the output of the coil. In addition to the number of turns of the coil, the difference in the width and thickness of the coil will also change the interaction of the coil with the magnetic field of the magnetic ball, so the magnetic flux change in the coil caused by the movement of the magnetic ball will be different, which will affect the power output [27,28]. The definitions of the coil width and thickness are shown in Figure 2. Using the control variable method, the effect of varying the thickness and width of the coil on the output was analyzed.

As shown in Figure 6, when the number of turns and the width of the coil were kept constant, the thickness of the coil was increased from 1 mm to 6 mm, and the peak value of the induced voltage was decreased from 2.57 V to 2.17 V. The results indicate that the thicker the coil, the more unfavorable it is for the output [11,29]. If the number of turns and

the thickness of the coil were kept constant and the width of the coil was increased from 0.75 cm to 4.5 cm, the peak value of the induced voltage decreased from 2.18 V to 1.48 V. The wider the coil, the more unfavorable it is to the output [20].
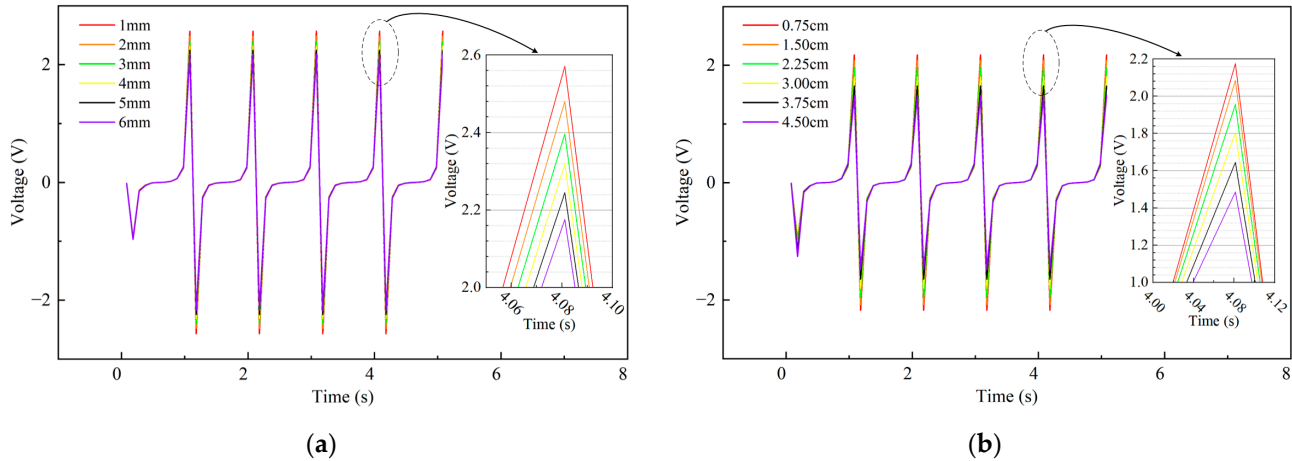

Figure 6. Law of the effect of coil thickness and width on output. (**a**) Output voltage at different coil thicknesses; (**b**) output voltage at different coil widths.

4. Experiment

4.1. Motion Analysis of A-EMG under Wave Action

The motion of the A-EMG under wave action was analyzed in order to develop an experimental program. In fact, the motion of waves in the ocean is particularly complex and variable, and it is not a simple periodic movement. The generation of waves in the ocean is essentially a vibration process in the ocean, and its motion can be regarded as a combination of countless disordered regular fluctuations. Due to the complexity of the causes of wave motion and the difficulty of using accurate mathematical models to make a precise description, in the analysis and design of machinery related to ocean engineering, researchers have always simplified the motion of waves to simple harmonic motion or to the superposition of simple harmonic motion in their studies. And, they often use the Airy linear wave theory to characterize the wave motion law in a general steady state situation [30,31]. Here, we also used the Airy linear wave theory to explain the wave principle. The profile of a wave is described by a simple harmonic curve [32], as show in Figure 7.
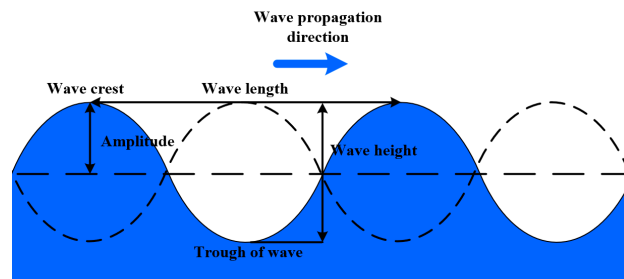

Figure 7. Airy linear wave theory model.

According to the Airy linear wave theory, the motion of a wave can be described by Equation (6).

$$\begin{cases} \eta(s,t) = \frac{H}{2}\cos(ks - \omega t) \\ k = \frac{2\pi}{L} \\ \omega = \frac{2\pi}{T} \end{cases} \tag{6}$$

where s is the displacement of the wave in the direction of horizontal motion, η is the elevation of the wave from the still water surface, H is the wave height, k is the wave

number, t is the time, ω is the frequency of the wave and T and L are the period and wavelength, respectively.

When a floating body is on the water surface, it will move with the waves, and the floating body will produce different forms of motion with the change in the wave parameters. Taking the *XOZ* plane as an example, Figure 8 shows a schematic diagram of waves with different parameters acting on the A-EMG in the *XOZ* plane, where φ is the angle between the wave's direction of action and the *X*-direction, so $tan\varphi$ is the derivative of the line between the zero point and the position of the A-EMG. The wave will cause the A-EMG to produce different forms of motion, which are mainly manifested in the form of reciprocal displacement motion in the direction of wave action, so φ also denotes the direction of motion of the A-EMG, and the tilt motion around the *Y*-axis, producing a constantly changing tilt angle θ with respect to the *X*-axis, and $tan\theta$ is the derivative of the wave at this point [17,33].
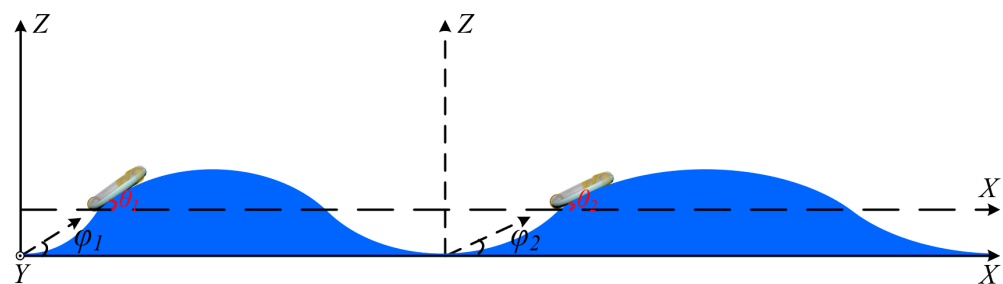

Figure 8. Wave action on the A-EMG.

Therefore, in this paper, a 6-DOF platform was used to simulate the motion of a floating body under the action of waves with different parameters. The control variable method was used to investigate the effects of the motion direction φ, amplitude, frequency and tilt angle θ of the A-EMG on the output and to explore the regular pattern.

4.2. Experimental Platform Construction

Based on the laws derived from the theoretical analysis and simulation results, an annular electromagnetic generator was fabricated. The specific parameters are shown in Table 2.

Table 2. Parameters in fabrication.

Item	Value
Outer diameter × inner diameter of annular shell	140 mm × 70 mm
Annular shell thickness	1 mm
Magnetic ball (N35) diameter	30 mm
Turns of coil	1000
Thickness × width of coil	3 mm × 15 mm
Volume of A-EMG	0.539×10^{-3} m^3

As shown in Figure 9, two identical semi-annular shells with an inner diameter of 70 mm and an outer diameter of 140 mm were fabricated by 3D printing. The annular shell needed to have sufficient hardness and to also leave room for the movement of the magnetic ball. The thickness of the shell was set to 1 mm in the 3D printing, so its internal space was 33 mm. After placing a 30 mm diameter N35 magnetic ball inside, three 0.1 mm enameled wire coils were wound along the radial direction of the annular shell, and the coils were equally spaced on the annular shell. With the coil width and number of turns set to 1.5 cm and 1000 turns, respectively, the thickness of the coil was approximately 3 mm. The volume of the A-EMG was calculated to be approximately 0.539×10^{-3} m^3, which includes the inner diameter of the annular shell and is the volume of the actual space occupied by the A-EMG. A TH2690 electrostatic meter was used as the data acquisition

device, and the 6-DOF platform was used as the external excitation device to simulate the wave motion. Figure 9 shows a schematic diagram of the overall experimental platform. The TH2690 electrometer is an integrated instrument that functions as a voltmeter, ammeter and electrometer, among other things. When measuring an open-circuit voltage and a short-circuit current, the probe of the instrument should simply be connected to the output terminal of the measured target, and the corresponding testing function should be selected.

(**a**)   (**b**)

Figure 9. A-EMG production and experimental platform construction. (**a**) A-EMG physical object; (**b**) experimental platform.

The 6-DOF platform consisted of two parts: a motion platform and a software control platform. The software control platform controlled the displacement and frequency of six linear motors in the motion platform, which could achieve linear motion along the *X*, *Y* and *Z* axes, respectively, in three-dimensional coordinates as well as rotational motion around the *X*, *Y* and *Z* axes, are denoted by α, β, γ respectively. It could also couple individual motion into composite motion. In the output testing section of this article, the motion effect of the waves in different directions, φ, acting on the A-EMG in the *XOZ* plane was achieved by coupling the motion of the platform along the *X* and *Z* axes, and the tilt angle of θ was achieved by setting the rotation around the *Y*-axis on the control platform. The method in this paper is more accurate and convenient than the method in reference [25,34], which used a single linear motor and manually changed the excitation direction.

4.3. Output Performance of the A-EMG

It should be noted that since the parameters of each group of coils were the same, their outputs ere similar, and the output of coil 1 will be used as an example to illustrate this. Firstly, the influence of the tilt angle was neglected, and the tilt angle was set to 0 using the 6-DOF platform. Through the coupling of the *X*-direction and the *Z*-direction, the motion form of the waves acting on the A-EMG in different directions in the *XOZ* plane was simulated, and the reciprocal displacement motions in the different directions were generated.

We collected the wave parameters from a certain sea area in China, where most of the wave heights are higher than 5 cm and the wave frequency near 5 cm is 1.2 Hz. By verifying that the A-EMG is able to work with small vibrations, we can show that it is able to work under most sea conditions. So, the frequency was set to 1.2 Hz, and the amplitude was set to 5 cm. The variation in the A-EMG with an open-circuit voltage and a short-circuit current with the motion direction φ is shown in Figure 10. As φ increased, the open-circuit voltage and short-circuit current of the A-EMG gradually decreased. When the value of φ reached 60°, the A-EMG could not generate electrical energy because the test only considered the influence of the reciprocating displacement motion, but the larger the wave action, φ, the easier it is to generate a larger tilt angle, θ [34]. Therefore, we also conducted an experimental test on the influence of the tilt angle on the output.
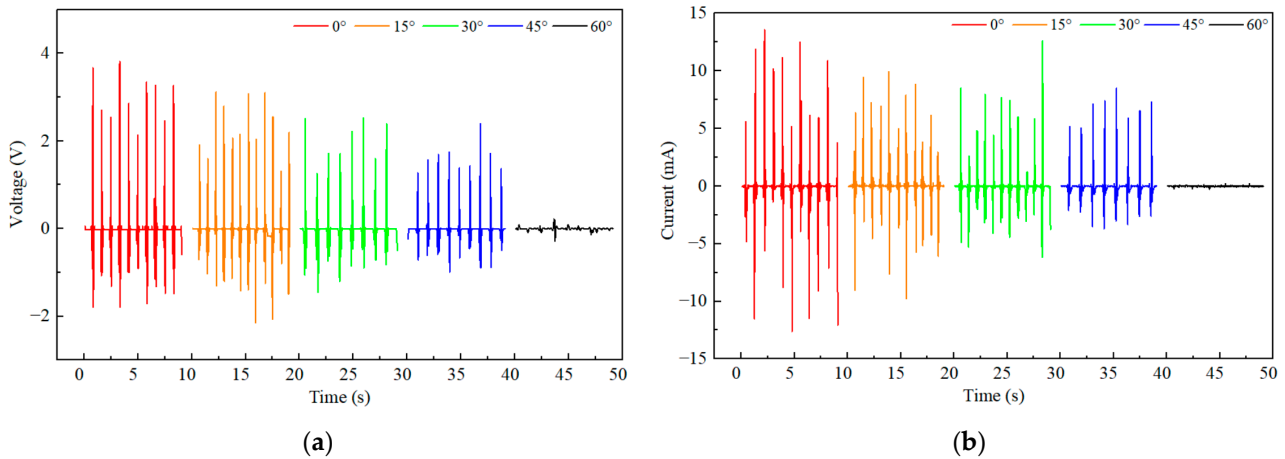
Figure 10. Open-circuit voltage and short-circuit current under the influence of motion direction, φ. (**a**) Open-circuit voltage; (**b**) short-circuit current.

If we want to make sure that the A-EMG can adapt to most wave conditions, we should first make sure that the A-EMG can work properly in a small angle range under smaller fluctuations. As shown in Figure 11, at a frequency of 1.2 Hz, when the tilt angle increased from 3° to 12°, there was no obvious effect on the output because the A-EMG is a centrosymmetric structure and the magnetic ball could easily resonate with the external excitation, making the magnetic ball perform a circular motion with the same frequency in the annular shell, which is in accordance with the theoretical derivation of Equation (5). However, it can be obviously observed in the experimental process that the larger the tilt angle, the more the ball in the A-EMG was stimulated to move, which compensated for the situation that the output of the reciprocating displacement motion was weakened when the wave action, φ, was increased; so, the device can collect wave energy from every direction.
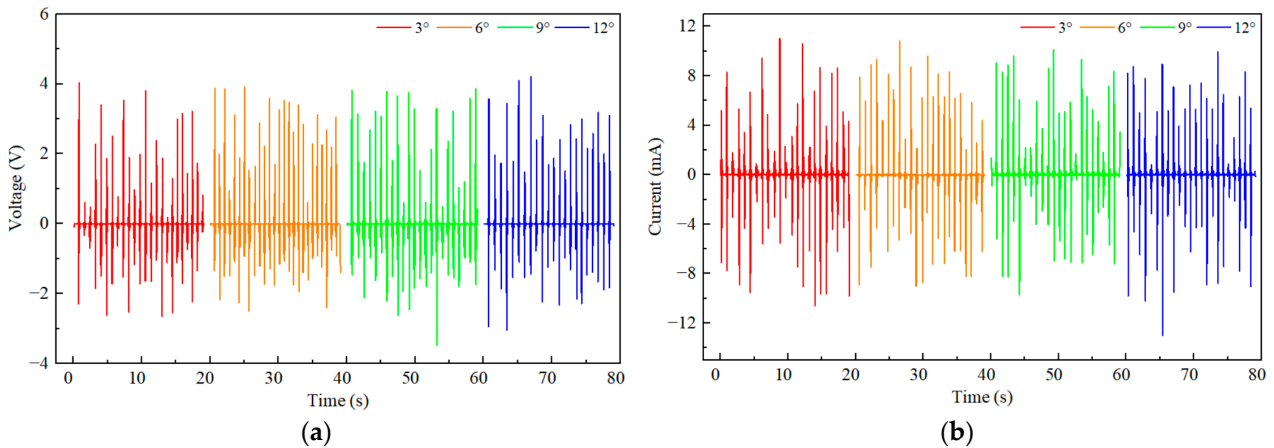

Figure 11. Open-circuit voltage and short-circuit current under the influence of tilt angle, θ. (**a**) Open-circuit voltage; (**b**) short-circuit current.

The frequency and amplitude are the most fundamental elements of waves. We tested the influence of the frequency and amplitude on the output of the A-EMG in the *X* direction (φ and θ were zero). As shown in Figure 12, when the amplitude was fixed, the maximum open-circuit voltage increased from 1.52 V to 7.2 V; as the frequency was increased from 1.0 Hz to 1.8 Hz, the maximum short-circuit current increased from 10.08 mA to 21.2 mA. As shown in Figure 13, when the frequency was fixed, the open-circuit voltage and short-circuit current were almost unchanged in the test range of 60 mm–120 mm. This was for the same reason that θ affected the output, which was also due to resonance.
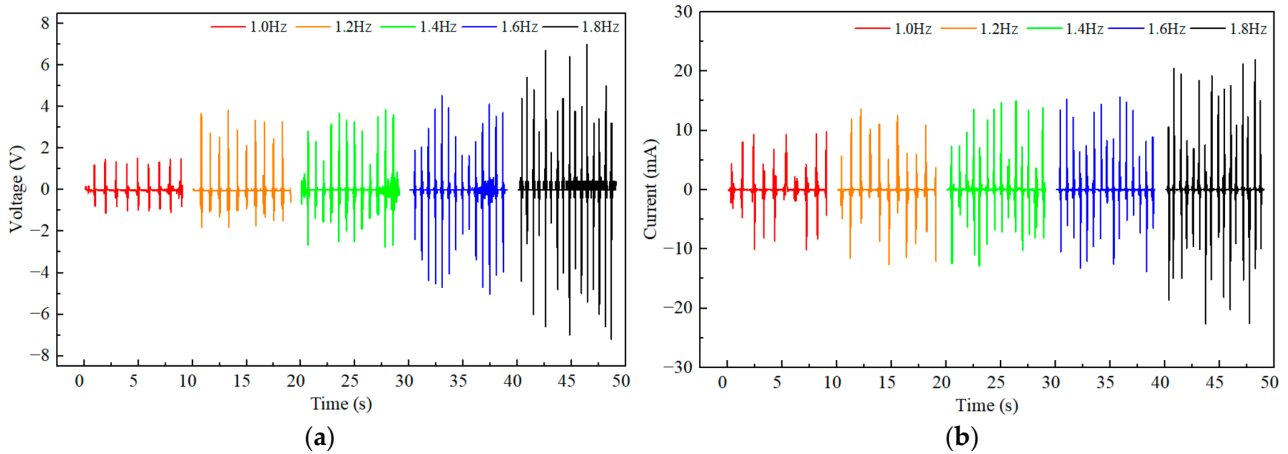
Figure 12. Open-circuit voltage and short-circuit current under the influence of frequency. (**a**) Open-circuit voltage; (**b**) short-circuit current.
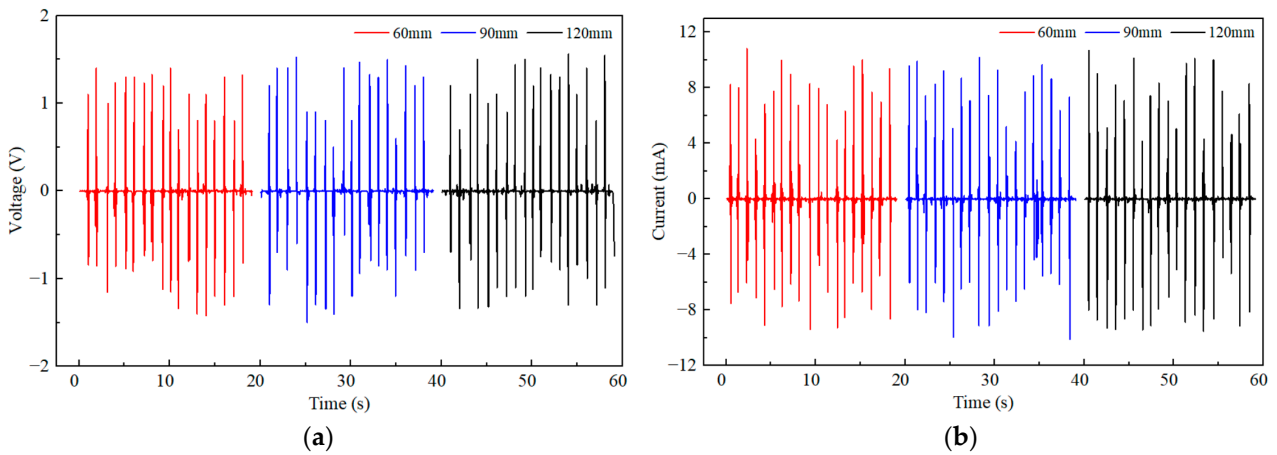

Figure 13. Open-circuit voltage and short-circuit current under the influence of amplitude. (**a**) Open-circuit voltage; (**b**) short-circuit current.

The optimum output power of the electromagnetic generator was found by impedance matching, where the output voltage was measured across various external resistors to study the optimum output power. Theoretically, when the load resistance is equal to the internal resistance of the electromagnetic generator, for the optimal output power, at this time, the relationship between the load voltage, V_L, and the open-circuit voltage, V_{OC}, is given by Equation (7).

$$V_L = \frac{1}{2}V_{OC} \tag{7}$$

In this paper, the voltage at different loads was tested to calculate the output power of the electromagnetic generator, as per Equation (8) [22,35].

$$P_{RMS} = \frac{U_{RMS}}{R_L} \tag{8}$$

where U_{RMS} is the root mean square (*RMS*) voltage on different load resistors, R_L is the load resistor and P_{RMS} is the optimal output power.

Tested at frequencies of 1 Hz and 1.8 Hz, respectively, as shown in Figure 14, the value of U_{RSM} of the external load increased with the increase in the load resistance, and the value of P_{RSM} first increased and then decreased with the increase in the load. Under both conditions, the maximum values of P_{RSM} obtained at an external load resistance of 150 Ω were 3.42 mW and 80.87 mW, respectively.
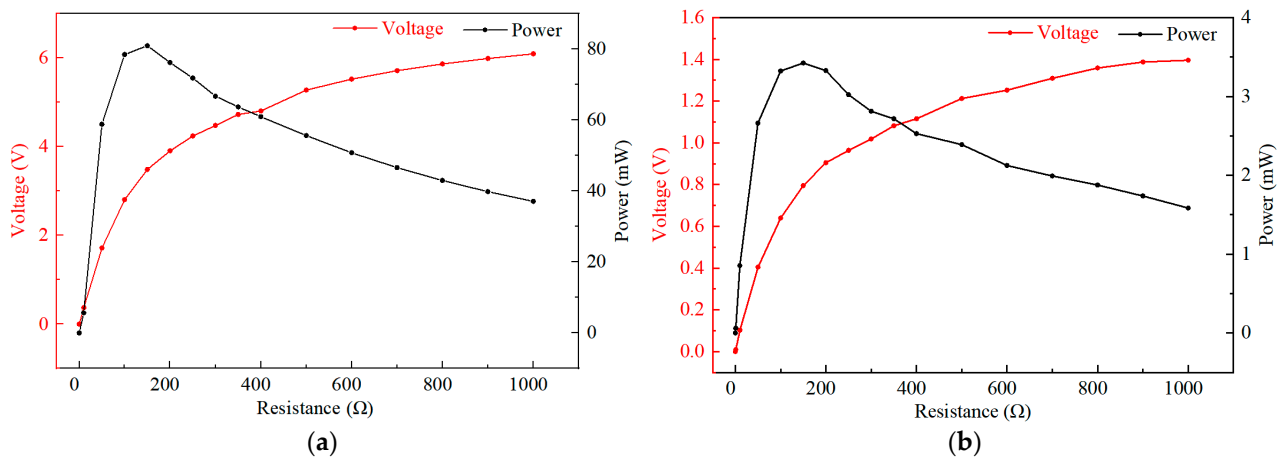
Figure 14. U_{RMS} and P_{RMS} at different external load resistances. (**a**) At 1.8 Hz excitation; (**b**) at 1 Hz excitation.

The maximum power density of the A-EMG can reach 150.174 W/m^3. Table 3 compares the performance of the A-EMG with existing wave energy harvesters [22]. Through comparison, it was found that the power density of the A-EMG has significant advantages.

Table 3. Comparison of different works.

Ref.	Type	Frequency (Hz)	Output Power (mW)	Power Density (W/m^3)
[32]	EMG + TENG	2.5	1.25	9
[35]	EMG + PZT	1.8	21.95	3.914
[22]	EMG	2.6	65	43.5
This work	EMG	1.8	80.87	150.174

Since the device generates AC power, which cannot directly power electronic devices, it must be rectified to DC power and stored in capacitors or batteries in order to provide stable power. The ability of energy harvesters to charge capacitors is an important index for evaluating their performance. At the same time, in order to verify the best connection mode between the coils, the output of each coil is rectified by a rectifier bridge and then connected in series or parallel to compare and study the effect of the two different connections on the charging characteristics of the capacitor. As shown in Figure 15, under the experimental conditions of the *X* direction and with 1.8 Hz excitation, the characteristics of charging the 22 µF capacitor were compared under three charging modes; one coil, three coils in series and three coils in parallel were compared. The circuit diagrams of the parallel and series charging modes of the three coils are shown in Figure 15a,b, respectively. Figure 15c. compares the three charging modes. It can be seen that multiple coils can charge the capacitor to a higher voltage in a relatively shorter time than a single coil, where three coils in parallel can charge the capacitor in the best way, being capable of charging the 22 µF capacitor to 8.6 V in 3.8 s.

To verify the application performance of the A-EMG, as shown in Figure 16, three coils were rectified and then connected in parallel to 25 parallel-connected commercial LED arrays, and single-degree-of-freedom wave motion modes, including the experimental conditions in this paper, and multiple-degree-of-freedom coupled wave motion modes, i.e., those shown in Table 4, were simulated by using a 6-DOF platform, and the LED arrays could be instantaneously lit under all these excitations.
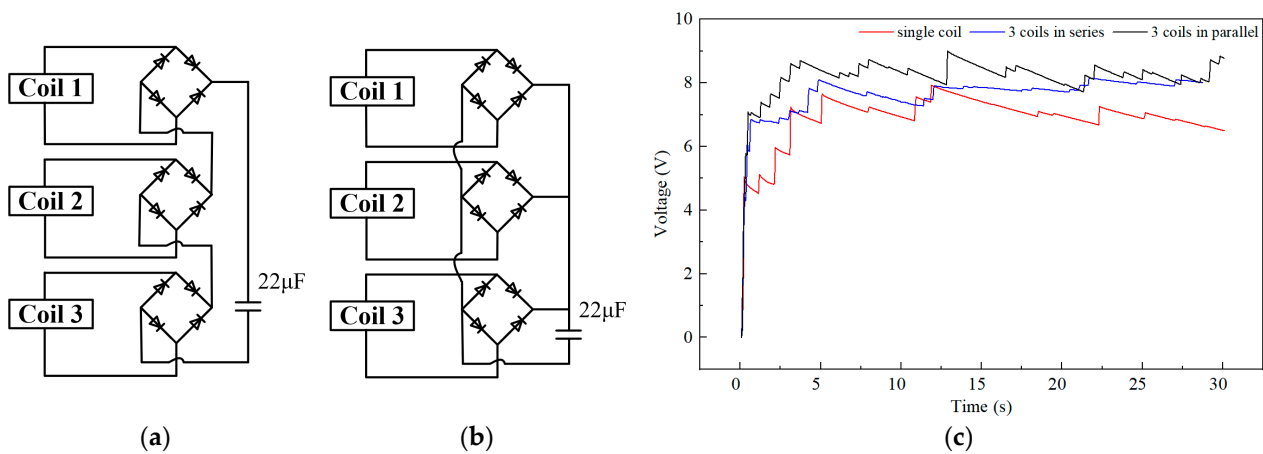
Figure 15. Capacitor charging with different connections between coils. (**a**) Series connection between coils; (**b**) parallel connection between coils; (**c**) comparison of different connections for capacitor charging.
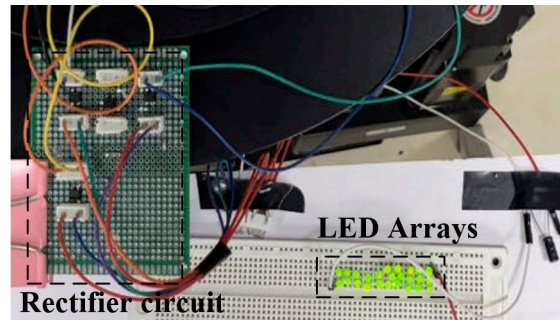

Figure 16. Application performance verification: lighting LED arrays.

Table 4. Parameters of simulating wave.

Direction	Frequency (Hz)	Amplitude (mm)	Tilt (°)
X, β coupling	1	50	3
Z, β coupling	1	50	3
X, Y coupling	1	50	-

5. Conclusions

In order to effectively harvest wave energy, this paper presents an annular electromagnetic generator for harvesting wave energy. The output performance of the three electromagnetic coil generating units was investigated. Under an external excitation of 1.8 Hz, the maximum open-circuit voltage of a single group of coils could reach 7.2 V, and the short-circuit current could reach 21.2 mA. An optimum output power of 80.87 mW was obtained when the external load was 150 Ω. The power density could reach 150.174 W/m^3. The output performance is superior to most wave energy collectors in the same field. Comparing the characteristics of the three coils after rectifying them to charge the capacitor in series or parallel, it was found that the parallel connection mode was the best, and a capacitor of 22 µF could be charged to 8.6 V in 3.8 s. Finally, the 6-DOF platform was used to simulate the typical motion characteristics of a wave, such as single-degree-of-freedom and multi-degree-of-freedom coupling, and to simulate lighting up an LED array. In summary, the device is simple in structure, low in terms of fabrication cost, responds well to the external excitation of wave energy, can continuously charge the capacitor and supply power to LED loads and has good application prospects in supplying power to ocean sensors.

Abbreviations

The following abbreviations are used in this manuscript:
A-EMG   Annular electromagnetic generator
6-DOF   Six-degree-of-freedom

References

1. Khan, F.A.; Pal, N.; Saeed, S.H. Review of solar photovoltaic and wind hybrid energy systems for sizing strategies optimization techniques and cost analysis methodologies. *Renew. Sustain. Energy Rev.* **2018**, *92*, 937–947. [CrossRef]
2. Nagura, M. Annual Rossby waves below the pycnocline in the Indian Ocean. *J. Geophys. Res. Ocean* **2018**, *123*, 9405–9415. [CrossRef]
3. Gemme, D.A.; Bastien, S.P.; Sepe, R.B.; Montgomery, J.; Grilli, S.T.; Grilli, A. Experimental testing and model validation for ocean wave energy harvesting buoys. In Proceedings of the 2013 IEEE Energy Conversion Congress and Exposition, Denver, CO, USA, 28 October 2013; pp. 337–343.
4. Pirisi, A.; Grimaccia, F.; Mussetta, M.; Zich, R.E.; Johnstone, R.; Palaniswami, M.; Rajasegarar, S. Optimization of an energy harvesting buoy for coral reef monitoring. In Proceedings of the 2013 IEEE Congress on Evolutionary Computation, Cancun, Mexico, 20–23 June 2013; pp. 629–634.
5. Zhang, Y.; Zhao, Y.; Sun, W.; Li, J. Ocean wave energy converters: Technical principle, device realization, and performance evaluation. *Renew. Sustain. Energy Rev.* **2021**, *141*, 110764. [CrossRef]
6. Ahamed, R.; McKee, K.; Howard, I. Advancements of wave energy converters based on power take off (PTO) systems: A review. *Ocean Eng.* **2020**, *204*, 107248. [CrossRef]
7. Hu, Y.; Yang, J.; Niu, S.; Wu, W.; Wang, Z.L. Hybridizing triboelectrification and electromagnetic induction effects for high-efficient mechanical energy harvesting. *ACS Nano* **2014**, *8*, 7442–7450. [CrossRef] [PubMed]
8. Arnold, D.P. Review of Microscale Magnetic Power Generation. *IEEE Trans. Magn.* **2007**, *43*, 3940–3951. [CrossRef]
9. Carneiro, P.; Soares Dos Santos, M.P.; Rodrigues, A.; Ferreira, J.A.; Simões, J.A.; Marques, A.T.; Kholkin, A.L. Electromagnetic energy harvesting using magnetic levitation architectures: A review. *Appl. Energy* **2020**, *260*, 114191. [CrossRef]
10. Bowers, B.J.; Arnold, D.P. Spherical, rolling magnet generators for passive energy harvesting from human motion. *J. Micromech. Microeng.* **2009**, *19*, 94008. [CrossRef]
11. Samad, F.A.; Karim, M.F.; Paulose, V.; Ong, L.C. A Curved Electromagnetic Energy Harvesting System for Wearable Electronics. *IEEE Sens. J.* **2016**, *16*, 1969–1974. [CrossRef]
12. Tu, D.; Zhang, Y.; Zhu, L.; Fu, H.; Qin, Y.; Liu, M.; Ding, A. A bistable vibration energy harvester with spherical moving magnets: Theoretical modeling and experimental validation. *Sens. Actuators A Phys.* **2022**, *345*, 113782. [CrossRef]
13. Graves, J.; Kuang, Y.; Zhu, M. Counterweight-pendulum energy harvester with reduced resonance frequency for unmanned surface vehicles. *Sensors Actuators A Phys.* **2021**, *321*, 112577. [CrossRef]
14. Yerrapragada, K.; Ansari, M.H.; Karami, M.A. Enhancing power generation of floating wave power generators by utilization of nonlinear roll-pitch coupling. *Smart Mater. Struct.* **2017**, *26*, 94003. [CrossRef]
15. Townsend, N.C. Self-powered autonomous underwater vehicles: Results from a gyroscopic energy scavenging prototype. *IET Renew. Power Gener.* **2016**, *10*, 1078–1086. [CrossRef]
16. Townsend, N.C.S.R. Gyrostabilizer Vehicular Technology. *Appl. Mech. Rev.* **2011**, *64*, 10801. [CrossRef]

17. Guo, Q.; Sun, M.; Liu, H.; Ma, X.; Chen, Z.; Chen, T.; Sun, L. Design and experiment of an electromagnetic ocean wave energy harvesting device. In Proceedings of the 2018 IEEE/ASME International Conference on Advanced Intelligent Mechatronics (AIM), Auckland, New Zealand, 9–12 July 2018; pp. 381–384.

18. Ding, W.; Song, B.; Mao, Z.; Wang, K. Experimental investigations on a low frequency horizontal pendulum ocean kinetic energy harvester for underwater mooring platforms. *J. Mar. Sci. Technol.* **2016**, *21*, 359–367. [CrossRef]

19. Lou, H.; Wang, T.; Zhu, S. Design, modeling and experiments of a novel biaxial-pendulum vibration energy harvester. *Energy* **2022**, *254*, 124431. [CrossRef]

20. Wang, Y.; Lee, C. Dynamics and power generation of wave energy converters mimicking biaxial hula-hoop motion for mooring-less buoys. *Energy* **2019**, *183*, 547–560. [CrossRef]

21. Carandell, M.; Toma, D.M.; Gasulla, M.; Rio, J.D. Experimental Validation of a Kinetic Energy Harvester Device for Oceanic Drifter Applications. In Proceedings of the IEEE OES/MTS OCEANS 2019-Marseille, Marseille, France, 17–20 June 2019; pp. 1–7.

22. Pan, X.; Ling, P.; Bao, H.; He, W.; Li, Q.; Yan, B. Tumbler-inspired electromagnetic generator for low-frequency ocean wave energy harvesting. *Energy Convers. Manag.* **2023**, *294*, 117569. [CrossRef]

23. Maharjan, P.; Toyabur, R.M.; Park, J.Y. A human locomotion inspired hybrid nanogenerator for wrist-wearable electronic device and sensor applications. *Nano Energy* **2018**, *46*, 383–395. [CrossRef]

24. Gao, L.; Lu, S.; Xie, W.; Chen, X.; Wu, L.; Wang, T.; Wang, A.; Yue, C.; Tong, D.; Lei, W.; et al. A self-powered and self-functional tracking system based on triboelectric-electromagnetic hybridized blue energy harvesting module. *Nano Energy* **2020**, *72*, 104684. [CrossRef]

25. He, J.; Fan, X.; Mu, J.; Wang, C.; Qian, J.; Li, X.; Hou, X.; Geng, W.; Wang, X.; Chou, X. 3D full-space triboelectric-electromagnetic hybrid nanogenerator for high-efficient mechanical energy harvesting in vibration system. *Energy* **2020**, *194*, 116871. [CrossRef]

26. Hao, C.; He, J.; Zhai, C.; Jia, W.; Song, L.; Cho, J.; Chou, X.; Xue, C. Two-dimensional triboelectric-electromagnetic hybrid nanogenerator for wave energy harvesting. *Nano Energy* **2019**, *58*, 147–157. [CrossRef]

27. Gao, S. Design and Implementation of a Piezoelectric and Magnetoelectric Vibration Energy Harvester. Master's Thesis, Harbin Institute of Technology, Harbin, China, 2017.

28. Wu, K. Research On Magnetic Spring Vertical Vibration Energy Harvesting Technology. Master's Thesis, Xidian University, Xi'an, China, 2013.

29. Vidal, J.V.; Rolo, P.; Carneiro, P.M.; Peres, I.; Kholkin, A.L.; dos Santos MP, S. Automated electromagnetic generator with self-adaptive structure by coil switching. *Appl. Energy* **2022**, *325*, 119802. [CrossRef]

30. Zhang, Y. Design and Analysis of Multi Degree of Freedom Wave Energy Power Generation Device. Master's Thesis, Shantou University, Shantou, China, 2021.

31. Tao, Y. Design and Analysis of Multi-Degree-of-Freedom Wave Power Generation System. Master's Thesis, Tianjin University, Tianjin, China, 2017.

32. Chen, X.; Gao, L.; Chen, J.; Lu, S.; Zhou, H.; Wang, T.; Wang, A.; Zhang, Z.; Guo, S.; Mu, X.; et al. A chaotic pendulum triboelectric-electromagnetic hybridized nanogenerator for wave energy scavenging and self-powered wireless sensing system. *Nano Energy* **2020**, *69*, 104440. [CrossRef]

33. Li, Y.; Ma, X.; Tang, T.; Zha, F.; Chen, Z.; Liu, H.; Sun, L. High-efficient built-in wave energy harvesting technology: From laboratory to open ocean test. *Appl. Energy* **2022**, *322*, 119498. [CrossRef]

34. Gao, X. Triboelectric Nanogenerator for Harvesting Multidirectional Water Wave Energy. Master's Thesis, Lanzhou University, Lanzhou, China, 2022.

35. Shi, G.; Zeng, W.; Xia, Y.; Xu, J.; Jia, S.; Li, Q.; Wang, X.; Xia, H.; Ye, Y. A floating piezoelectric electromagnetic hybrid wave vibration energy harvester actuated by a rotating wobble ball. *Energy* **2023**, *270*, 126808. [CrossRef]